



**POLITECNICO**  
**MILANO 1863**

SCUOLA DI INGEGNERIA INDUSTRIALE  
E DELL'INFORMAZIONE



## Simulation of a LEO orbiting microsat on Simulink

MSc IN SPACE ENGINEERING

### Authors:

10723712	MARCELLO PARESCHI	(BSc AEROSPACE ENGINEERING - POLITECNICO DI MILANO)
10836125	DANIELE PATERNOSTER	(BSc AEROSPACE ENGINEERING - POLITECNICO DI MILANO)
10711624	ALEX CRISTIAN TURCU	(BSc AEROSPACE ENGINEERING - POLITECNICO DI MILANO)
10884250	TAMIM HARUN OR	(BSc AEROSPACE ENGINEERING - INTERNATIONAL ISLAMIC UNIVERSITY MALAYSIA)

Professor: FRANCO BERNELLI ZAZZERA

Academic year: 2023-2024

---

## Abstract

The following report discusses the attitude dynamics and control of a microsatellite in Sun-synchronous low-Earth orbit. The mission of the satellite is to point the Earth, due to the payload requirement. The simulation was carried out in Simulink environment. The rotational dynamics was modeled through the Euler equations, the kinematics was parametrized through two sets of Euler angles (312 - 313). The environment disturbances that was accounted for were the magnetic field interaction and gravity gradient torque. They were considered the most relevant after a general analysis of all the four main disturbances (SRP, air drag torque, magnetic torque, gravity gradient torque). The orbital motion was modeled as a restricted two body problem.

The on-board sensors were a horizon sensor, a magnetometer and a sun sensor. They were all modeled in Simulink, taking as reference real sensors. The actuators installed on the satellite were a magnetorquer and two reaction wheels, modeled referring to real actuators.

The control logic implemented on-board considers two algorithms. The first deals with the de-tumbling of the spacecraft using the B-dot control, until a certain condition on the value of the derivative of B is satisfied. The second contemplates the slew and tracking manoeuvre together. This last phase is performed through an extension of the PD controller for non-linear dynamics.

## Contents

<b>Abstract</b>	<b>I</b>
<b>Contents</b>	<b>II</b>
<b>1 Symbols</b>	<b>III</b>
1.3 Framework analysis . . . . .	III
1.4 Dynamics . . . . .	III
1.5 Kinematics . . . . .	III
1.6 Disturbances analysis . . . . .	III
1.7 Sensors . . . . .	III
1.8 Attitude determination . . . . .	III
1.9 Actuators . . . . .	IV
1.10 Control logic . . . . .	IV
1.11 Simulation results . . . . .	IV
<b>2 Requirements</b>	<b>1</b>
<b>3 Framework Analysis</b>	<b>1</b>
3.1 Satellite characterization . . . . .	1
3.2 Orbit characterization . . . . .	1
<b>4 Dynamics</b>	<b>3</b>
<b>5 Kinematics</b>	<b>3</b>
<b>6 Disturbances analysis</b>	<b>4</b>
6.1 Magnetic Disturbance . . . . .	4
6.2 SRP Disturbance . . . . .	4
6.3 Drag Disturbance . . . . .	5
6.4 Gravity Gradient Disturbance . . . . .	5
6.5 Simulation of all disturbances . . . . .	6
<b>7 Sensors</b>	<b>7</b>
7.1 Horizon Sensor . . . . .	7
7.2 Magnetometer . . . . .	7
7.3 Sun Sensor . . . . .	8
<b>8 Attitude determination</b>	<b>8</b>
<b>9 Actuators</b>	<b>10</b>
9.1 Magnetorquers . . . . .	10
9.2 Reaction Wheels . . . . .	11
<b>10 Control logic</b>	<b>11</b>
10.1 De-tumbling phase: the B-dot control . . . . .	12
10.2 Slew and Nadir pointing phases . . . . .	13
10.2.1 Control law for the Slew and Tracking Manuever . . . . .	13
10.2.2 Actuator command logic for Slew and Nadir pointing . . . . .	14
<b>11 Simulation results</b>	<b>15</b>
11.1 Detumbling analysis . . . . .	16
11.2 Slew and tracking phase analysis . . . . .	16
11.3 Control action analysis . . . . .	17
<b>Bibliography</b>	<b>20</b>

## 1. Symbols

### 1.3. Framework analysis

$I$	$[kg/m^2]$	inertia matrix
$a$	$[km]$	semi-major axis
$e$	$[-]$	eccentricity
$i$	$[deg]$	inclination
$\omega$	$[deg]$	pericentre anomaly
$\Omega$	$[deg]$	RAAN
$\theta$	$[rad]$	true anomaly
$n$	$[rad/s]$	mean anomaly
$\mathcal{P}$	$[-]$	perifocal frame
$\mathcal{N}$	$[-]$	inertial frame
$A_{PN}$	$[-]$	rotation matrix from inertial to perifocal frame
$r_p$	$[km]$	S/C position in $\mathcal{P}$ frame
$r_N$	$[km]$	S/C position in $\mathcal{N}$ frame

### 1.4. Dynamics

$\mathcal{B}$	$[-]$	body frame
$x_b$	$[-]$	x direction of the $\mathcal{B}$ frame
$y_b$	$[-]$	y direction of the $\mathcal{B}$ frame
$z_b$	$[-]$	z direction of the $\mathcal{B}$ frame
$\omega$	$[rad/s]$	angular velocity in $\mathcal{B}$ frame
$\dot{\omega}$	$[rad/s]$	angular velocity rate in $\mathcal{B}$ frame
$M_d$	$[Nm]$	disturbances torque
$M_c$	$[Nm]$	control torque

### 1.5. Kinematics

$s$	$[rad]$	set of Euler angles
$\dot{s}$	$[rad/s]$	set of Euler angle's rates
312	$[-]$	sequence of axis' rotation
313	$[-]$	sequence of axis' rotation
$\phi$	$[rad]$	first rotation's angle
$\theta$	$[rad]$	second rotation's angle
$\psi$	$[rad]$	third rotation's angle
$A_{BN}$	$[Nm]$	attitude matrix
$tol$	$[-]$	tolerance value for singularity check

### 1.6. Disturbances analysis

$M$	$[Nm]$	disturbance torque
$D$	$[Am^2]$	magnetic dipole from coils or parasitic currents
$B$	$[T]$	magnetic field
$V$	$[Tm]$	magnetic field scalar potential
ECEF	$[-]$	Earth Centered Earth Fixed frame
$r$	$[m]$	radial distance from Earth's centre to S/C position (ECEF)
$\theta$	$[rad]$	longitude (ECEF)
$\phi$	$[rad]$	co-latitude (ECEF)
$P^{n,m}(\cos \theta)$	$[-]$	Gauss normalized associated Legendre functions
$g^{n,m}(t)$	$[nT]$	Schmidt semi-normalized spherical harmonic coefficients
$h^{n,m}(t)$	$[nT]$	Schmidt semi-normalized spherical harmonic coefficients

$F_i$	$[N]$	disturbance force acting on i-th panel
$P$	$[Pa]$	Sun's pressure of radiation
$A_i$	$[Pa]$	area of i-th panel
$\hat{S}_B$	$[-]$	Sun's direction in $\mathcal{B}$ frame
$\hat{N}_{B,i}$	$[-]$	i-th panel's normal direction in $\mathcal{B}$ frame
$\rho_s$	$[-]$	coefficient of specular reflection
$\rho_a$	$[-]$	coefficient of absorption
$\rho_d$	$[-]$	coefficient of diffusion
$\epsilon$	$[deg]$	obliquity of Earth
$C_D$	$[-]$	coefficient of drag
$r_i$	$[m]$	position of centre of action of the force
$v_{B,i}$	$[m/s]$	relative velocity in $\mathcal{B}$ frame of the i-th panel
$\hat{v}_{B,i}$	$[s^{-1}]$	direction of relative velocity in $\mathcal{B}$ frame of the i-th panel
$\rho$	$[kg/m^3]$	density of air
$\rho_0$	$[kg/m^3]$	reference density of air from US Standard Atmosphere model (1976)
$h_0$	$[km]$	reference height from US Standard Atmosphere model (1976)
$H$	$[km]$	scaling height from US Standard Atmosphere model (1976)
$G$	$[m^3 kg^{-1} s^{-2}]$	universal gravitational constant
$m_t$	$[kg]$	mass of Earth
$c_i$	$[-]$	director cosines of the radial direction in the $\mathcal{B}$ frame

### 1.7. Sensors

$N_p$	$[rad^2 s]$	noise power
$T_s$	$[s]$	sampling time
$\sigma^2$	$[rad^2]$	variance of the measurement
$N.S.D.$	$[nT/\sqrt{Hz}]$	noise spectral density
$I$	$[A]$	intensity of current
$\alpha$	$[A/W]$	coefficient of the sun sensor
$S$	$[m^2]$	sensor's surface area
$W$	$[W/m^2]$	intensity of incident radiation
$\theta$	$[rad]$	angle of incident light

### 1.8. Attitude determination

$J$	$[-]$	cost function
$\alpha_i$	$[-]$	weight on i-th sensor for J function
$s_i$	$[-]$	unit vector measured by sensor in $\mathcal{B}$ frame
$v_i$	$[-]$	unit vector calculated by on-board model in $\mathcal{N}$ frame
$\phi$	$[rad]$	error angle between true and measured direction without bias

$E[\phi]$	[rad]	expected value of error angle
$\sigma_\phi^2$	[rad <sup>2</sup> ]	variance of error angle
$\sigma_\phi$	[rad]	standard deviation of error angle

### 1.9. Actuators

$D$	[Am <sup>2</sup> ]	magnetic dipole from magnetorquers
$M$	[Nm]	control torque
$h$	[kgm <sup>2</sup> /s]	angular momentum of wheels + satellite
$h_r$	[kgm <sup>2</sup> /s]	relative angular momentum of reaction wheel
$\dot{h}_r$	[kgm <sup>2</sup> /s <sup>2</sup> ]	relative angular momentum rate of reaction wheel
$\omega_{max}$	[RPM]	saturation speed of reaction wheel
$\dot{h}_{max}$	[Nm]	maximum available torque for reaction wheel
$\omega_r$	[rad/s]	relative angular velocity of reaction wheel
$\dot{\omega}_r$	[rad/s <sup>2</sup> ]	relative angular velocity rate of reaction wheel
$\sigma_\omega$	[RPM]	standard deviation on $\omega_r$

### 1.10. Control logic

$B_B$	[T]	magnetic field in $\mathcal{B}$ frame
$\dot{B}_B$	[1/s]	magnetic field rate unit direction in $\mathcal{B}$ frame
$k_\omega$	[kg · m <sup>2</sup> /s]	gain for detumbling phase
$\dot{A}_{BN}$	[1/s]	rate of attitude matrix
$B_N$	[T]	magnetic field in $\mathcal{N}$ frame
$\dot{B}_N$	[T/s]	magnetic field rate in $\mathcal{N}$ frame

$\mathcal{LVCH}$	[–]	local vertical local horizontal frame
$A_{BL}$	[–]	error matrix between $\mathcal{B}$ and $\mathcal{LVCH}$ frame
$\xi$	[deg]	angle between orbital plane and magnetic equator
$\epsilon$	[–]	attitude error for non-linear control
$\omega_{BL}$	[rad/s]	angular velocity error between $\mathcal{LVCH}$ and $\mathcal{B}$ frames
$k_1$	[kg · m <sup>2</sup> /s <sup>2</sup> ]	gain on attitude error for non-linear control
$k_2$	[kg · m <sup>2</sup> /s]	gain on angular velocity error for non-linear control
$\alpha$	[rad]	small Euler angles between $\mathcal{B}$ and $\mathcal{LVCH}$ frame
$\dot{\alpha}$	[rad/s]	small Euler angles rate between $\mathcal{B}$ and $\mathcal{LVCH}$ frame
$K_p$	[kg · m <sup>2</sup> /s <sup>2</sup> ]	gain matrix on $\alpha$ for linear control
$K_d$	[kg · m <sup>2</sup> /s]	gain matrix on $\dot{\alpha}$ for linear control
$K_x$	[–]	yaw inertial coefficient
$K_y$	[–]	roll inertial coefficient
$p_{open}$	[1/s]	open-loop poles for the dynamic system
$p$	[1/s]	closed-loop poles for the dynamic system

### 1.11. Simulation results

$B_m$	[T]	measured magnetic field
$\ \dot{B}_m\ $	[1/s]	norm of rate of change of direction of $B_m$
$\omega_{estim}$	[rad/s]	onboard estimation of angular velocity

## 2. Requirements

	Assigned specification	Modifications	Motivation for modifications
<b>Platform</b>	Microsat	-	-
<b>Attitude parameters</b>	Euler angles	-	-
<b>Sensor</b>	Earth Horizon	Magnetic, Sun	Magnetic because of magnetorquers Sun because no eclipse during orbit
<b>Actuator</b>	3 magnetorquers	2 reaction wheels	Underactuation of magnetorquers

Table 1: Mandatory requirements for the project

## 3. Framework Analysis

### 3.1. Satellite characterization

The satellite design was inspired by ESAIL, a microsatellite developed by exactEarth in cooperation with ESA. ESAIL was primarily developed for ship targeting.<sup>[1]</sup> Two configurations of the satellite were implemented: the undeployed configuration for the detumbling phase and the extended configuration for the slew and tracking phase. The deployed configuration is modeled as a cubic central body of side 70 cm and four solar panels, modeled as rectangular bodies of dimensions  $70 \times 70 \times 1$  cm. Solar panels are set along  $y_B$  axis of body frame  $\mathcal{B}$  with the normal of surface parallel to  $z_B$  axis, as shown in Figure 1.

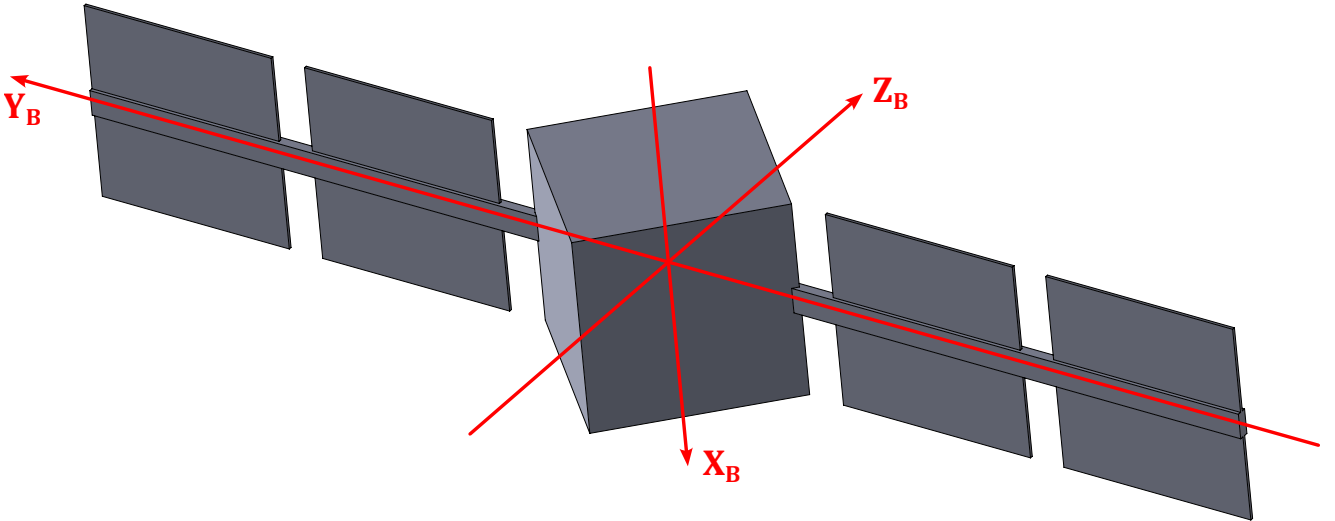


Figure 1: CAD model of the satellite

The mass is assumed to be 100 kg with isotropic distribution for simplicity. The inertia matrix results to be:

$$I = \begin{bmatrix} 22.9724 & 0 & 0 \\ 0 & 7.7770 & 0 \\ 0 & 0 & 23.1895 \end{bmatrix} \text{ kg/m}^2 \quad (1)$$

The undeployed configuration is an isotropic cube of side 70 cm with the same mass. The inertia matrix of this undeployed configuration is then:

$$I = \begin{bmatrix} 8.1667 & 0 & 0 \\ 0 & 8.1667 & 0 \\ 0 & 0 & 8.1667 \end{bmatrix} \text{ kg/m}^2 \quad (2)$$

### 3.2. Orbit characterization

The orbit adopted for the simulation is a nearly polar, LEO, Sun-synchronous orbit (SSO). Polar orbits allows to scan the whole globe during the several orbits thanks to Earth's rotation. SSO are orbits that maintain the same angle

between their orbital plane and the direction that connects the Earth with the Sun<sup>[2]</sup>. This allows the spacecraft to monitor the Earth surface with the same conditions of light (or eventually darkness, if the plane is oriented in a certain way). Furthermore, a SSO can be selected to ensure constant visibility of the Sun.<sup>[3]</sup>

The orbital data are based on the ephemeris of an ESA mission taken at 12:00 UT on December 16th, 2023. The orbit was then propagated using the simple two-body problem without any perturbations.

This is an approximation as several disturbances act on the satellite (as discussed in section 6). Using the ephemeris as the initial condition has the advantage of allowing the simulation of spacecraft motion in two or three periods of the orbit to be considered as Sun-synchronous. This is because the time of simulation is a snapshot compared to the time of action of the J2 effect responsible for the Sun-synchronous orbit, which is one year. Clearly, a more detailed simulation should consider the variation of the orbital parameters due to J2 and all the other perturbations.

The orbital parameters chosen as described above are the following:

$a$ [km]	$e$ [-]	$i$ [deg]	$\omega$ [deg]	$\Omega$ [deg]
6851	0.0018	97.40	101.58	0

Table 2: Orbital parameters

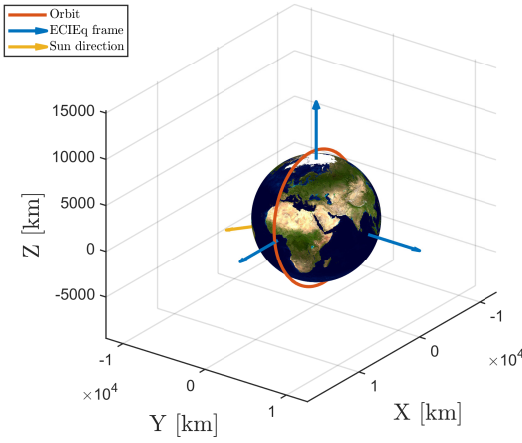


Figure 2: Orbit representation

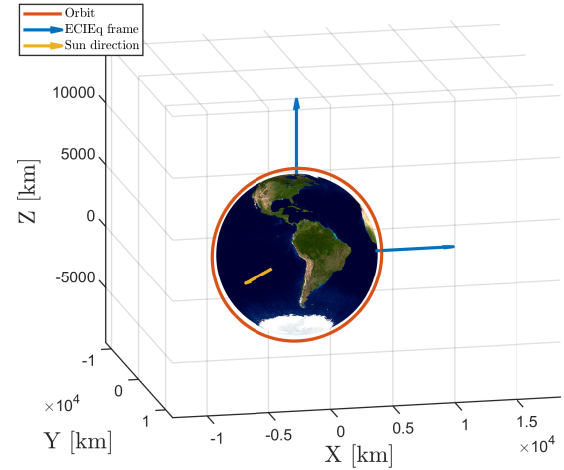


Figure 3: View from Sun direction

In Figure 2 and Figure 3 the Sun direction is plotted. This direction was computed by taking the ephemeris of the Earth with respect to the Sun at 12:00 UT December 16th in the Earth centered Equatorial frame. Since the orbital periods considered are relatively small compared to the Sun's motion, its position was maintained constant during the simulation. It's easy to see that the orbit never goes into eclipse condition.

On Simulink, the model implemented to retrieve the orbital position is based on the integration of the true anomaly:

$$\dot{\theta} = \frac{n(1 + e \cos \theta)^2}{(1 - e^2)^{3/2}} \quad (3)$$

Then, the radial distance is computed as:

$$r = \frac{a(1 - e^2)}{1 + e \cos \theta} \quad (4)$$

At this point it is easy to retrieve the position  $\mathbf{r}_P$  of the satellite in the perifocal frame  $\mathcal{P}$ :

$$\mathbf{r}_P = r \begin{bmatrix} \cos \theta \\ \sin \theta \\ 0 \end{bmatrix} \quad (5)$$

The position in the inertial frame  $\mathcal{N}$  is calculated using the transpose of the rotation matrix  $\mathbf{A}_{PN} = \mathbf{R}_3(\omega) \mathbf{R}_1(i) \mathbf{R}_3(\Omega)$ :

$$\mathbf{r}_N = \mathbf{A}_{PN}^T \mathbf{r}_P \quad (6)$$

## 4. Dynamics

The equations of the dynamics adopted for the rotating rigid body motion are the Euler equations. The set of equations are referred to the principal inertia axis frame of the satellite. This frame coincides with the body frame  $\mathcal{B}$  previously defined (subsection 3.1). It is described by three unit vectors  $\{x_B, y_B, z_B\}$  that are in the direction of principal inertia axis of the satellite.

$$I\dot{\omega} + \omega \times I\omega = M_d + M_c \quad (7)$$

In Equation 7 the external torque is split into two contributions.  $M_d$  describes the disturbance torques acting on the spacecraft due to environment, it is treated in more detail in section 6.  $M_c$  is referred to the control torque that the actuators generate in order perform the tasks required by the control logic (see section 10).

With particular reference to the Simulink model, the two different configurations of the satellite are considered: undeployed configuration for detumbling phase and extended configuration for slew and tracking. Since the inertia matrix of the system must switch from Equation 2 to Equation 1, a logic switch has been implemented during the simulation, using a flag based on the activation of the detumbling control. This instantaneous switch is not completely realistic since the extraction of the panels would require some finite time and could influence the real dynamic of the satellite. Anyhow, for the microsat considered, the retracted configuration allows a faster detumbling and also reduces the inertia loads and stresses on the solar panels and the structure.

## 5. Kinematics

As specified in section 2, the attitude parameters of the satellite are expressed through the use of Euler angles. The kinematics calculated according to this parameterization follows these steps:

- given the angular velocity  $\omega$  from dynamics for each time and the initial condition on Euler angles  $s_0$ , compute the time derivatives of the angles  $\dot{s}$ ;
- integrate the derivatives to obtain the set of Euler angles  $s$  for each time;
- from the calculated angles, compute the attitude matrix  $A_{BN}$ .

When dealing with this type of parameterization, a major issue arises due to the singularity conditions on the second angle  $\theta$  for any chosen set of three Euler angles. This can cause the derivatives of the other two angles to tend towards infinity. The problem is a result of the fact that, under these specific conditions, the set of Euler angles is not uniquely defined, as the first and third rotations are performed on the same physical direction.

To avoid these singularities, it becomes necessary to have two systems working on two different sets of Euler angles:

- one set of angles defined by three different indexes, which has the singularity condition on  $\theta = (2n + 1)\pi/2$ ;
- one set of angles where the first and the last indexes coincide, which has the singularity condition on  $\theta = n\pi$ ;

with  $n \in \mathbb{N}$ . To merge these two systems and avoid singularities, there are two main options:

- run both systems all the time, get the attitude kinematics only from one system until it reaches its singularity condition on  $\theta$ , then switch to the other system, which will be further from its singularity;
- run just one system at a time; when the system reaches its singularity condition, convert from the current set of angles to the other set through the attitude matrix, impose the calculated angles as initial condition on the other system, then start the integration from where it was interrupted, deactivating the system that reached the singularity.

Although the first option is simpler, the second option offers significant computational savings for the simulation. It is important to note that the kinematics model is only executed in the simulation to calculate the satellite's motion over time and is not executed on the satellite processor. Despite the added complexity of the system switch, the second option was chosen to accelerate the execution of the Simulink model.

In the model discussed in this report, the 312 and 313 sets of Euler angles were chosen. The equations for the integration and the conversion to attitude matrix are reported below:

$$\begin{aligned} \begin{cases} \dot{\phi}_{312} = \frac{\omega_z \cos \psi - \omega_x \sin \psi}{\cos \theta} \\ \dot{\theta}_{312} = \omega_x \cos \psi + \omega_z \sin \psi \\ \dot{\psi}_{312} = \omega_y - (\omega_z \cos \psi - \omega_x \sin \psi) \tan \theta \end{cases} & A_{312} = \begin{bmatrix} \cos \psi \cos \phi - \sin \psi \sin \phi \sin \theta & \cos \psi \sin \phi + \sin \psi \cos \phi \sin \theta & -\sin \psi \cos \theta \\ -\sin \phi \cos \theta & \cos \phi \cos \theta & \sin \theta \\ \sin \psi \cos \phi + \cos \psi \sin \phi \sin \theta & \sin \psi \sin \phi - \cos \psi \cos \phi \sin \theta & \cos \theta \cos \psi \end{bmatrix} \\ \begin{cases} \dot{\phi}_{313} = \frac{\omega_x \sin \psi + \omega_y \cos \psi}{\sin \theta} \\ \dot{\theta}_{313} = \omega_x \cos \psi - \omega_y \sin \psi \\ \dot{\psi}_{313} = \omega_z - (\omega_x \sin \psi + \omega_y \cos \psi) \cot \theta \end{cases} & A_{313} = \begin{bmatrix} \cos \psi \cos \phi - \sin \psi \sin \phi \cos \theta & \cos \psi \sin \phi + \sin \psi \cos \phi \cos \theta & \sin \psi \sin \theta \\ -\sin \psi \cos \phi - \cos \psi \sin \phi \cos \theta & -\sin \psi \sin \phi + \cos \psi \cos \phi \cos \theta & \cos \psi \sin \theta \\ \sin \phi \sin \theta & -\cos \phi \sin \theta & \cos \theta \end{bmatrix} \end{aligned} \quad (8)$$

In order to translate one set of Euler angles to the other set is sufficient to remember that  $A_{312}$  must be equal to  $A_{313}$ , since attitude matrices are both related to the same physical object. Inverting the formulas:



$$\begin{cases} \phi_{312} = \text{atan2}(-A^{2,1}, A^{2,2}) \\ \theta_{312} = \arcsin(A^{2,3}) \\ \psi_{312} = \text{atan2}(-A^{1,3}, A^{3,3}) \end{cases} \quad \begin{cases} \phi_{313} = \text{atan2}(A^{3,1}, -A^{3,2}) \\ \theta_{313} = \arccos(A^{3,3}) \\ \psi_{313} = \text{atan2}(A^{1,3}, A^{2,3}) \end{cases} \quad (9)$$

The system switcher has been designed in Simulink using basic boolean operators. These operators are combined to generate a 'flag' signal that selects the appropriate system, taking into account the singularity conditions of both. In more detail, the switcher logic takes as input three boolean signals:

- $|\cos \theta_{312}| < \text{tol}$ , where  $\text{tol}$  is a chosen tolerance value to keep the 312 system distant from the singularity;
- $|\sin \theta_{313}| < \text{tol}$ , where  $\text{tol}$  is a chosen tolerance value to keep the 313 system distant from the singularity;
- the **flag** of the system at the previous step time.

A truth table can be created using the given signals and expected output. The truth table can then be simplified using basic logic operators such as AND, OR, and NOT through boolean algebra. Finally, the logic can be implemented in the simulation to handle the activation of the two systems.

## 6. Disturbances analysis

In order to make a realistic simulation of the rotating motion of the spacecraft, the disturbances caused by the environment must be taken into account. The following paragraphs provide a brief introduction to the main disturbances acting on the system. The simulation results for the chosen satellite and orbit will then be presented to aid in the selection of the two most significant disturbances. Since the other disturbances are typically much smaller than the dominant ones (often by some orders of magnitude), they will be disregarded in the final simulation.

### 6.1. Magnetic Disturbance

The influence of the Earth's magnetic field on the satellite is relevant due to the proximity of the orbit taken in exam. Besides the crucial role that it plays in the actuation, the magnetic field could also cause relevant disturbances on the satellite's dynamics. The magnetic torque, whether generated by the magnetorquers or by parasitic currents present in the satellite, follows the general law:

$$\mathbf{M} = \mathbf{D} \times \mathbf{B} \quad (10)$$

where  $\mathbf{D}$  is the magnetic dipole generated by a coil or by parasitic currents,  $\mathbf{B}$  is the magnetic field vector.

A mathematical model of the magnetic field is necessary to evaluate  $\mathbf{B}$  given the satellite position along the orbit. The model chosen for the purpose is the 13th edition of the International Geomagnetic Reference Field (IGRF). According to this model, the magnetic field  $\mathbf{B}$  is evaluated as the gradient of a magnetic scalar potential  $V$ , which is modelled as a spherical harmonic expansion of order  $N$ :

$$\mathbf{B}(r, \theta, \phi, t) = -\nabla V(r, \theta, \phi, t) \quad V(r, \theta, \phi, t) = a \sum_{n=1}^N \sum_{m=0}^n \left(\frac{a}{r}\right)^{n+1} (g^{n,m}(t) \cos m\phi + h^{n,m}(t) \sin m\phi) P^{n,m}(\cos \theta) \quad (11)$$

where  $r, \theta, \phi$  are the spherical coordinates of the satellite in a Earth-Centered Earth-Fixed (ECEF) frame,  $a$  is the Earth's equatorial radius (6371.2 km),  $P^{n,m}(\cos \theta)$  are the Gauss normalized associated Legendre functions,  $g^{n,m}(t)$  and  $h^{n,m}(t)$  are the Schmidt semi-normalized spherical harmonic coefficients. These coefficients are computed from experimental data and depend on time, as the Earth magnetic field is not constant but changes significantly every year. In this simulation, the coefficients refer to year 2020 of IGRF-13 and the expansion is computed up to order 13. Note that the model must be in the ECEF frame because the magnetic field rotates with the Earth. To adapt the model to an Earth-Centered Inertial (ECI) frame, a rotation matrix is required for the input and its transpose for the output. The matrix takes account of the angular velocity of Earth on time. Lastly, the magnetic field  $\mathbf{B}$  can be expressed in the body frame through the attitude matrix.

Once that  $\mathbf{B}$  is defined for every satellite position, the  $\mathbf{D}$  vector is chosen as an arbitrary constant (based on typical microsat values) and the torque is easily computed along the orbit thanks to [Equation 10](#).

### 6.2. SRP Disturbance

The Solar Radiation Pressure (SRP) torque is the disturbance generated by electromagnetic waves that impact on the spacecraft panels generating force. These forces acting on some of the panels can rise a net torque around the center of mass of the spacecraft. For this analysis, only the Sun radiation is considered, while a more rigorous study should also consider the infrared radiation emitted by the Earth and the radiation of the Sun reflected by the Earth. Moreover, no eclipse condition is analyzed during the simulation, which is a reasonable assumption given the SSO chosen in [subsection 3.2](#).

The formula to calculate the force acting on each discrete panel  $i$  is the following:



$$\mathbf{F}_i = -PA_i (\hat{\mathbf{S}}_B \cdot \hat{\mathbf{N}}_{B,i}) \left[ (1 - \rho_s) \hat{\mathbf{S}}_B + \left( 2\rho_s (\hat{\mathbf{S}}_B \cdot \hat{\mathbf{N}}_{B,i}) + \frac{2}{3}\rho_d \right) \hat{\mathbf{N}}_{B,i} \right] \quad (12)$$

In order to simulate this kind of disturbance, the coefficients of absorption  $\rho_a$ , specular reflection  $\rho_s$  and diffusion  $\rho_d$  must be decided. Since these three parameters are related through an energetic balance as  $\rho_a + \rho_d + \rho_s = 1$ , only two of them are independent while the third follows. These values clearly depends on the material of the main body and the solar panels of the spacecraft. In order to determine the force on each surface, the geometry of the panels of the satellite must be given (subsection 3.1), in particular the surface of each panel  $S_i$  and direction of the normal of the panel  $\hat{\mathbf{N}}_{B,i}$  expressed in  $\mathcal{B}$  frame. The direction of Sun  $\hat{\mathbf{S}}_B$  is modeled in ECI frame considering the obliquity  $\epsilon = 23.44$  deg of Earth's rotation axis with respect to the ecliptic plane, then it is rotated in  $\mathcal{B}$  frame through the attitude matrix.

Lastly, to be able to compute the torque it must be known where the resulting force acts on each panel (i.e. the centre of SRP force of the panel). It is assumed as a first approximation that the forces act on the geometric center of the corresponding plate. In order to correctly calculate the total torque, a shadow check must be performed. This has been implemented in Simulink by checking the sign of the dot product between the normal versor of the plate  $\hat{\mathbf{N}}_{B,i}$  and the Sun direction  $\hat{\mathbf{S}}_B$ .

### 6.3. Drag Disturbance

Over extended periods, the spacecraft's engagement with the higher strates of Earth's atmosphere results in the generation of a torque around its center of mass. At altitudes less than 400 kilometers, the aerodynamic torque is usually the predominant factor, though its significance diminishes considerably beyond 700 kilometers of altitude. For the simulation, the geometry of the panels is defined in subsection 3.1. The coefficient of drag  $C_D$  is set to 2.2, the relative velocity considers both the rotation of Earth around its axis and the rotation motion of the spacecraft. As for the SRP case (subsection 6.2), a sort of shadow check has been implemented based on the dot product between the relative velocity and the normal of the surface. This check is necessary since only the exposed-to-air surfaces give the contribution to generate the drag force. As for SRP torque, the position of the center of action of the force  $\mathbf{r}_i$  should be evaluated for each panel. As a first approximation, the resulting force is placed in the geometric center of the panel.

$$\mathbf{M} = \begin{cases} \sum_{i=1}^n \mathbf{r}_i \times \mathbf{F}_i & \text{if } \hat{\mathbf{N}}_{B,i} \cdot \hat{\mathbf{v}}_{B,i}^{rel} \geq 0 \\ \mathbf{0} & \text{if } \hat{\mathbf{N}}_{B,i} \cdot \hat{\mathbf{v}}_{B,i}^{rel} < 0 \end{cases} \quad \text{with} \quad (13)$$

$$\mathbf{F}_i = -\frac{1}{2}\rho C_D \|\mathbf{v}_{B,i}^{rel}\|^2 (\hat{\mathbf{N}}_{B,i} \cdot \hat{\mathbf{v}}_{B,i}^{rel}) A_i \hat{\mathbf{v}}_{B,i}^{rel} \quad n = \text{number of faces}$$

The air density  $\rho$  is computed according to the US Standard Atmosphere of 1976. The model uses an exponential law to describe  $\rho$  as a function of altitude  $h$ :

$$\rho = \rho_0 \cdot \exp \left[ -\frac{h - h_0}{H} \right] \quad (14)$$

Considering the orbit defined in subsection 3.2, the range of altitude is between 450 and 500 km. From this information, the constants of the formula are the following<sup>[4]</sup>:

$$\rho_0 = 1.585 \cdot 10^{-12} \text{ kg/m}^3 \quad h_0 = 450 \text{ km} \quad H = 60.828 \text{ km}$$

### 6.4. Gravity Gradient Disturbance

Since the gravity around the spacecraft is not uniform, a non-negligible gravity torque will arise from there. Studying the torque generated by an elementary force acting on the elementary mass  $dm$  the equation for this is obtained:

$$d\mathbf{M} = -\mathbf{r} \times \frac{Gm_t dm}{\|\mathbf{R} + \mathbf{r}\|^3} (\mathbf{R} + \mathbf{r}) \quad (15)$$

where  $\mathbf{r}$  is the position vector of  $dm$  from the center of mass and  $\mathbf{R}$  is the position vector of the center of mass from the center of Earth. Approximating this equation, and expressing the position vector of the centre of mass as the product of magnitude ( $R$ ) with the direction cosines, it's possible to centre this torque in the principal inertia axes. Integrating this equation the final form is achieved.

$$\begin{aligned}
M_x &= \frac{3Gm_t}{R^3} (I_z - I_y) c_2 c_3 \\
M_y &= \frac{3Gm_t}{R^3} (I_x - I_z) c_1 c_3 \\
M_z &= \frac{3Gm_t}{R^3} (I_y - I_x) c_1 c_2
\end{aligned} \tag{16}$$

The  $c_1, c_2$  and  $c_3$  are the direction cosines of the radial direction in the principal axes. Therefore if one of the principal axes is aligned with the radial direction the torque will be zero because only one of the direction cosines is non-zero. It's clear that this disturbance acts in a continuous manner throughout the orbit motion and the torque produced depends mainly on the attitude matrix.

Instead, the stability configuration depends on the distribution of mass of the spacecraft with respect to the target orientation. For our case of study, inspired by the ESAIL mission from ESA, the satellite is nadir pointing. In particular the  $x_b$  direction has to be aligned with the nadir, while the  $z_b$  has to be normal with respect to the orbital plane. Using the numerical values of the spacecraft, and the orientation requirements just mentioned this particular configuration results unstable to GG disturbance.

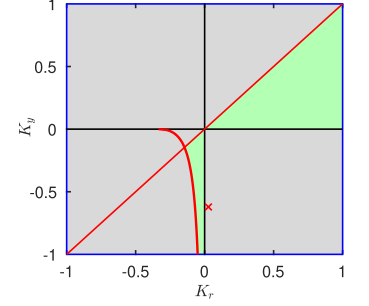


Figure 4: GG stability of satellite

### 6.5. Simulation of all disturbances

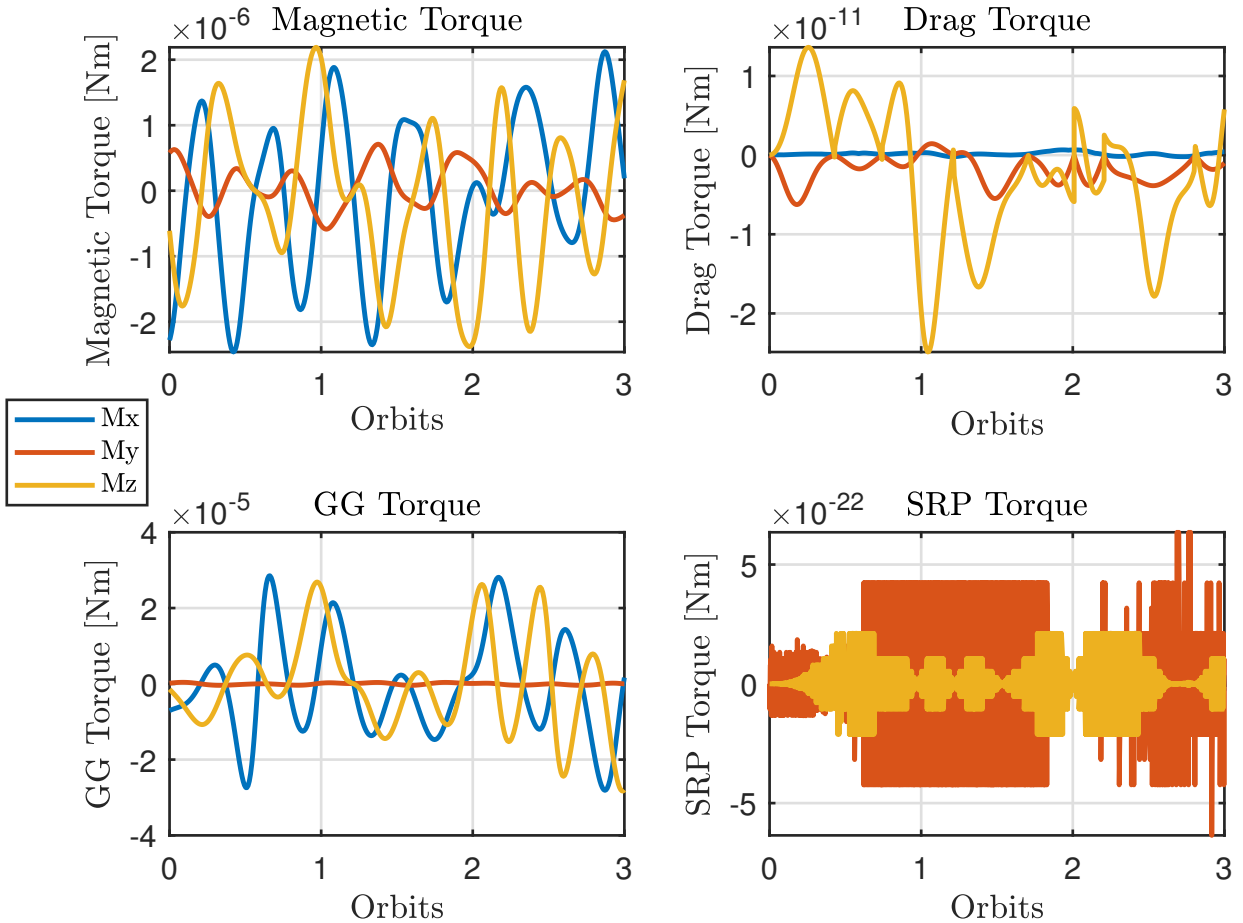


Figure 5: Simulation of all disturbances

The control-free motion has been simulated with all the disturbances for three full periods. The initial condition were set to null initial angular velocity and null Euler angles in the 312 set.

From the graphs of [Figure 5](#) it is clear that SRP disturbance is negligible in our case, the graph shows only numerical zeros. In particular, this is due to the symmetry of the geometry of the spacecraft, a small set off of the centre of mass would have produced a net torque. It is clear, that in this specific case, the two most relevant disturbances are due to magnetic field interaction and the gravity gradient torque since the atmospheric drag torque is some orders of magnitude smaller.

Note that in the Gravity Gradient torque the y-axis component is almost null compared to the other components along x and z, this is due to the fact that the y-axis component of the torque depends on the difference between inertia moment along x and along z, for our case those two moments of inertia are very similar (see [subsection 3.1](#)).

## 7. Sensors

Sensors are fundamental tools that allows the SC to know its orientation or angular velocity. Their presence onboard is fundamental for having a controlled motion of the satellite. In this section the three sensors used will be presented, it will be also clarified the motivation that lead the team to choose two additional sensors over the horizon sensor assigned.

### 7.1. Horizon Sensor

Horizon sensors are devices that can detect the centre of the planet, in our case Earth, and reconstruct the direction of that point with respect to the satellite. They usually work by analyzing the IR spectrum of the image through a thermopile to reduce the visible light spectrum interference caused by transition of day and night on earth. Due to the nadir pointing requirment a static earth sensor has been chosen for this specific application. In particular, the *Meisei Earth Horizon* was chosen, which has the following specifics<sup>[5]</sup>:

<i>F.O.V.</i> [deg]	<i>Accuracy</i> [deg]	<i>Frequency</i> [Hz]
33	1	30

Table 3: Real data for Horizon Sensor

Due to operational requirements, the static sensor has to point the Earth, in particular the optical axis must have the same direction of the nadir (direction that links centre of earth and CoM of the S/C). To fulfill this request, a good option could be to position the sensor on the face that also contains the payload, that is the face of the spacecraft main body (cube) that has normal along the  $x_b$  direction.

The model implemented to simulate the behaviour of the sensor in the Simulink environment takes the real position of the S/C with respect to centre of Earth expressed in inertial space, changes its direction multiplying by -1 and expresses it in the  $\mathcal{B}$  frame through the real attitude matrix  $A_{BN}$ . This unit vector is the input of the sensor block, here it is sampled through a zero-order hold of frequency specified by [Table 3](#) to simulate the digital nature of the sensor. Then some errors of measurments has to be added. It was decided to model two typical effects of real sensor: the mounting error that cause misalignment and also an accuracy error modeled with a band-limited white noise on all the components of the direction vector. Chronologically, first the misalignment is calculated, then the noise is introduced:

- The misalignment error was computed on Simulink by introducing a small deviation with respect to the nominal condition. This can be done by adding a small-scaled vector in the direction perpendicular of the unit vector that has to be measured. The scaling of this vector has to be small with respect to the unit direction considered as the measurment. Since the vector of the measured direction is initially unitary, the length of the bias vector introduced can be considered as  $\tan \theta_{small} \approx \theta_{small}$ , where  $\theta_{small}$  represents the angle between real measurment and misaligned measurment. The  $\theta_{small}$  selected is ...
- In the Simulink environment the white noise has to be defined through the noise power. This was selected as  $N_p = \sigma^2 T_s$ , where  $\sigma^2$  represents the variance as the standard deviation squared, while  $T_s$  is the sampling time of the sensor. It was decided to consider as standard deviation the value of 1 deg (that is the accuracy from [Table 3](#))

### 7.2. Magnetometer

Due to the LEO orbit and seen that from [subsection 6.5](#) the magnetic field was considered as one of the main disturbances, it was thought that a magnetometer could have been a sensor to implement on-board the satellite. This kind of sensor are in general less accurate than optical sensor as sun sensor or star sensor, but since the magnetic field of LEO orbit is effectively enough strong, the sensor can provide always a measurment. Also, having a magnetorquer assigned as mandatory, the coupling of this actuator with a magnetometer can be exploited during the de-tumbling maneuver since a direct dipole command is produced by the so-called *B-dot Control*, extensively discussed in [subsection 10.1](#).

The fluxgate magnetometer typology is used, where for each body axis, two ferromagnetic cores are used parallel to the specific axis. The primary coil saturates the two bars alternatively in opposite direction, so that the secondary

output theoretically can read a null induced voltage output produced by the time-varying flux. When external field is present, the symmetry of the alternate saturation is broken so that a shift on the magnetic flux of the secondary coil is produced. This net flux can be read by the time-history of a voltmeter on the secondary coil, since the spacing of the measured output voltage depends on the external magnetic field value.

Since magnetometer are usually characterized by low accuracy values, a deep search has been conducted to find a high-accuracy and low-noise typology. A suitable sensor is the *MM200* furnished by *AAC ClydeSpace*. The following performance parameters characterize the sensor:

<i>N.S.D</i> [ <i>nT</i> / $\sqrt{\text{Hz}}$ ]	<i>Frequency</i> [Hz]
1.18	30

Table 4: Real data for Magnetometer Sensor

For the Simulink model, the same approach of the Horizon sensor in subsection 7.1 has been used. In particular, the magnetic field vector from the block of subsection 6.1 has been transformed into the  $\mathcal{B}$  reference frame through the attitude matrix from the true kinematics block section 5. This is the input vector that has to be sampled with a frequency specified by Table 4. For this case a range of frequencies can be chosen: it was used the same frequency of the horizon sensor from Table 3 since it respects the constraint given by the magnetometer requirements.

Then the measurements errors have to be added, a first misalignment error modeled in the same way of the horizon sensor in subsection 7.1. For this case the perpendicular vector has been scaled by a factor of (...). The accuracy error, induced by the noise, has been modeled through a band-limited white noise added on each component. The value of  $N_p$  is the square of NSD presented in Table 4.

### 7.3. Sun Sensor

Sun sensors are devices that detect the position of the Sun by measuring the incidence angle of its radiation on a sensor surface. This surface is typically made of materials that can generate a current proportional to the intensity of the incident light. From the measure of the current  $I$  generated by the sensor surface of area  $S$ , knowing the intensity of the radiation  $W$  and the coefficient  $\alpha$  of the sensor, the angle of the incident light  $\theta$  is internally computed as:

$$I = \alpha S W \cos \theta \implies \theta = \arccos\left(\frac{I}{\alpha S W}\right) \quad (17)$$

The unit vector pointing towards the Sun can be easily computed by the sensor using the knowledge of two angles obtained by placing two surfaces on different directions on the same plane.

As discussed in section 3, the satellite mission consists in pointing the Earth on a Sun-synchronous orbit without any eclipse periods. Therefore, accuracy should be prioritised over having the best Field of View (FOV) when selecting the sensor. For this reason, the choice falls upon a small and light Fine Sun sensor with good performances such as the *AAC Clyde Space SS200*<sup>[6]</sup>:

<i>F.O.V.</i> [deg]	<i>Accuracy</i> [deg]	<i>Frequency</i> [Hz]
90	0.3	30

Table 5: Real data for Sun Sensor

This sensor has to be placed in the same direction as the solar panels (i.e. in the  $\mathbf{z}_b$  direction) so the Sun is constantly visible (since the orbit is Sun-synchronous). To avoid unnecessary complexity in the Simulink model, the sensor's field of view is not taken into consideration. This is because the sensor is not used during the detumbling manoeuvre, and in the tracking phase, the Sun is always visible. To simulate the output of the real sensor, the model uses the Sun direction calculated by adding the initial Earth-Sun vector to the position vector of the satellite in the inertial frame, which is computed through Keplerian dynamics. The resulting vector is then normalized, reversed, and transformed into the body frame using the attitude matrix. From here, errors have been added in the same manner as described for the horizon sensor (subsection 7.1).

## 8. Attitude determination

The problem of estimating the attitude matrix from the available measurements is central to spacecraft control. To determine the attitude of the spacecraft, the sensor models introduced earlier were used. The method used to determine the attitude is the SVD method<sup>[7]</sup>, which has been developed within the framework of Wahba's problem. The latter consists in finding the orthogonal matrix which minimizes the weighted cost function:

$$J(\mathbf{A}_{BN}) = \frac{1}{2} \sum_{i=1}^N \alpha_i \|\mathbf{s}_i - \mathbf{A}_{BN} \mathbf{v}_i\|^2 \quad (18)$$

in which  $\{\mathbf{s}_i\}$  is a set of the  $N$  measured unit vectors in body frame and  $\{\mathbf{v}_i\}$  the corresponding set of unit vectors in the inertial frame, computed using the on-board models. The set of weights  $\{\alpha_i\}$  was chosen basing on the relative accuracy of each sensor. It was assumed that the weight vector  $\alpha$  is normalized to 1, i.e.  $\sum_{i=1}^N \alpha_i = 1$ . This method needs at least two available measurements, so it works also in the case that the Earth is outside the FOV of the horizon sensor.

Since  $\mathbf{A}_{BN}$  is a orthogonal matrix and  $\mathbf{s}_i$  and  $\mathbf{v}_i$  are unit vectors, with some simple algebraic passages, the expression of  $J$  can be rewritten as:

$$J(\mathbf{A}_{BN}) = 1 - \sum_{i=1}^N \alpha_i (\mathbf{s}_i^T \mathbf{A}_{BN} \mathbf{v}_i) \quad (19)$$

The optimal solution minimizes  $J$ , therefore maximizes:

$$\tilde{J}(\mathbf{A}_{BN}) = \sum_{i=1}^N \alpha_i (\mathbf{s}_i^T \mathbf{A}_{BN} \mathbf{v}_i) = \text{Tr}(\mathbf{A}_{BN} \mathbf{B}^T) \quad (20)$$

where  $\text{Tr}$  is the trace operator and  $\mathbf{B} = \sum_{i=1}^N \alpha_i \mathbf{s}_i \mathbf{v}_i^T$ .

Since a direct solution is computationally expensive, a single value decomposition technique is used. The matrix  $\mathbf{B}$  can be decomposed as:

$$\mathbf{B} = \mathbf{U} \mathbf{S} \mathbf{V}^T = \mathbf{U} \text{diag}([s_1 \ s_2 \ s_3]) \mathbf{V}^T \quad (21)$$

$\mathbf{U}$  and  $\mathbf{V}$  are orthogonal matrices, representing the matrices of eigenvectors of  $\mathbf{B} \mathbf{B}^T$  and  $\mathbf{B}^T \mathbf{B}$  respectively,  $\mathbf{S}$  is the diagonal matrix containing the square roots of the eigenvalues of  $\mathbf{B}^T \mathbf{B}$ . Also other two matrices can be defined:

$$\mathbf{U}_+ = \mathbf{U} \text{diag}([1 \ 1 \ \det(\mathbf{U})]) \quad \text{and} \quad \mathbf{V}_+ = \mathbf{V} \text{diag}([1 \ 1 \ \det(\mathbf{V})]) \quad (22)$$

Then:

$$\mathbf{B} = \mathbf{U}_+ \mathbf{S}' \mathbf{V}_+^T = \mathbf{B} = \mathbf{U}_+ \text{diag}([s_1 \ s_2 \ s'_3]) \mathbf{V}_+^T \quad (23)$$

where:

$$s'_3 = s_3 \det(\mathbf{U}) \det(\mathbf{V}) \quad (24)$$

Now it can be defined the matrix  $\mathbf{W}$  and its representation in terms of Euler axis/angle:

$$\mathbf{W} = \mathbf{U}_+^T \mathbf{A} \mathbf{V}_+ = \cos\theta \mathbf{I}_3 - \sin\theta [\mathbf{e} \times] + (1 - \cos\theta) \mathbf{e} \mathbf{e}^T \quad (25)$$

$$\text{Tr}(\mathbf{A} \mathbf{B}^T) = \text{Tr}(\mathbf{W} \mathbf{S}') = \mathbf{e}^T \mathbf{S}' \mathbf{e} + \cos\theta (\text{Tr}(\mathbf{S}') - \mathbf{e}^T \mathbf{S}' \mathbf{e}) \quad (26)$$

The trace is maximized for  $\theta = 0$ , which gives  $\mathbf{W} = \mathbf{I}_3$  and thus the optimal attitude matrix is:

$$\mathbf{A} = \mathbf{U}_+ \mathbf{V}_+^T = \mathbf{U} \text{diag}([1 \ 1 \ \det(\mathbf{U}) \det(\mathbf{V})]) \mathbf{V}^T \quad (27)$$

Since sensor's measurements are affected by noise, a discrete low-pass Butterworth filter was added just after the calculation of the attitude matrix. The cut-off frequency was set to 0.5 rad/s for a 2nd order filter.

As previously mentioned, the weights required to construct the  $\mathbf{B}$  matrix are determined by the relative accuracy of each sensor. As no data regarding the magnetometer's accuracy in degrees was provided, the following procedure was implemented to assess its relative accuracy and assign a weight to each sensor. A period of three orbits was simulated, assuming to be already in the tracking phase, in order to be sure to be in the FOV of the Earth horizon sensor. During the simulation it was computed the angle  $\phi$  between the ideal unit vector and the measured one. For instance, when discussing the magnetometer,  $\phi$  represents the angle between the unit vector parallel to the magnetic field and the unit vector measured by the magnetometer. For each sensor  $\phi$  is a random number, it was then computed the expected value and the standard deviation with the formulas reported below:

$$E[\phi] = \frac{1}{3T} \int_0^{3T} \phi dt \quad \sigma_\phi^2 = \frac{1}{3T} \int_0^{3T} (\phi - E[\phi])^2 dt \quad \sigma_\phi = \sqrt{\sigma_\phi^2} \quad (28)$$

where  $T$  is the period of the orbit. The integrals were evaluated numerically. The results obtained are reported in Table 6:

<i>Sensor</i>	$E[\phi]$ [deg]	$\sigma_\phi$ [deg]
<i>Magnetometer</i>	0.0089	0.0078
<i>Sun Sensor</i>	0.3124	0.2720
<i>Earth Sensor</i>	1.1301	0.8544

Table 6: Expected value and standard deviation calculated

Basing on the previous results, it were chosen the weights  $\alpha_1$  used in the attitude determination with three sensors and  $\alpha_2$  used in the attitude determination with two sensors. The values are reported in Table 7:

<i>Sensor</i>	$\alpha_1$ [-]	$\alpha_2$ [-]
<i>Magnetometer</i>	0.80	0.80
<i>Sun Sensor</i>	0.15	0.20
<i>Earth Sensor</i>	0.05	–

Table 7: Weights  $\alpha_1$  and  $\alpha_2$

## 9. Actuators

### 9.1. Magnetorquers

Magnetorquers are actuators capable of inducing a torque on the spacecraft through the generation of a magnetic dipole, according to Equation 10. This dipole can be generated by an electrical current flowing into a coil, as stated in the Ampere-Maxwell equation from electromagnetism. To be capable of generating a  $\mathbf{D}$  vector in any direction of 3D space, three coils have to be placed on three perpendicular axis in order to generate three independent components of the magnetic dipole.

Magnetorquers are probably the most used attitude control actuators nowadays. This is primarily due to their extreme versatility and inexpensiveness for little satellites orbiting sufficiently near to Earth. All this combined with their virtually unlimited lifetime (because they only need current which can come from solar energy) give the magnetorquer a wide range of applicability. This comes clearly with some downsides. The most limiting factor for this type of actuator is the low torque generated, typically in the range of  $10^{-3} \div 10^{-6}$  Nm, that could render the control action really slow, especially for more big and heavy satellites.

Another limiting factor is of course the fact that they rely completely on the external magnetic field, which could vary a lot during the orbit and there could be zones in which the effectiveness is greatly reduced due to a weak  $\mathbf{B}$  vector. Furthermore, the satellite could be a source of disturbance due to some parasite currents flowing in other electronic devices. The same could be said for the magnetic coils themselves, which can be source of disturbance for the magnetic sensors.

In addition of all this, the torque generated by these actuators cannot have three independent components, since the torque can be generated only in a plane perpendicular to the  $\mathbf{B}$  of the magnetic field. This can be demonstrated from the Equation 10, which is reported and expanded below:

$$\mathbf{M} = \mathbf{D} \times \mathbf{B} = [-\mathbf{B} \times] \mathbf{D} \implies \begin{bmatrix} M_x \\ M_y \\ M_z \end{bmatrix} = \begin{bmatrix} 0 & B_z & -B_y \\ -B_z & 0 & B_x \\ B_y & -B_x & 0 \end{bmatrix} \begin{bmatrix} D_x \\ D_y \\ D_z \end{bmatrix} \quad (29)$$

$$\mathbf{D} = [-\mathbf{B} \times]^{-1} \mathbf{M} \quad (30)$$

Since  $[-\mathbf{B} \times]$  is a singular matrix, it cannot be inverted as shown in Equation 30, so the complete controllability of the system through magnetic actuators is not assured. For this reason, as the satellite is not GG stable (as shown in subsection 6.4) and the chosen orbit presents important variations of the  $\mathbf{B}$  vector during the simulation, the actuation has been integrated with two reaction wheels (more details in subsection 10.2.2).

The magnetorquer that was selected for this project is the *MTQ800* from *ACC Clyde Space*, which details are reported below<sup>[8]</sup>:



$D_{max} [Am^2]$	$frequency [Hz]$
15	30

Table 8: Real data for Magnetorquer

The Simulink model takes as input the ideal dipole requested by the controller, elaborates it through a rate limiter and a saturation limiter, then it introduces some random white noise. This model, which has been used also for the other actuators, is designed to replicate the accuracy, the dynamics and the limits of the actuators in the real world. Otherwise, the control would be ideal and it could generate some torques that would be impossible to obtain with physical actuators.

## 9.2. Reaction Wheels

Reaction wheels are one of the primary attitude control actuators for controlling the spacecraft, as they are reliable and can give precise pointing. Their working principle is based on the internal angular momentum exchange between the satellite and the reaction wheel itself. At every time instant, the angular momentum of the overall system composed by the reaction wheel and the rest of the satellite can be expressed as:

$$\mathbf{h} = I\boldsymbol{\omega} + \mathbf{h}_r \quad (31)$$

where  $\mathbf{h}_r$  is the angular momentum of the reaction wheel with respect to the rest of the spacecraft along its spin axis. If no external torque is applied, due to the conservation of angular momentum, it can be written:

$$I\dot{\boldsymbol{\omega}} = -\dot{\mathbf{h}}_r \quad (32)$$

Usually  $\dot{\mathbf{h}}_r$  is due to the torque applied to the reaction wheel by an electric motor, that has its proper operational curve. The latter can be modeled as constant until a certain angular velocity  $\omega_{max}$  is reached by the reaction wheel. When the saturation speed  $\omega_{max}$  is achieved, the reaction wheel cannot provide any additional torque, either positive or negative. If the torque required is more or less periodic, it is possible to choose the actuator in order to have it always in the functioning regime. If, in addition to the periodical component, there is a secular contribution, then it is inevitable to reach the saturation speed. To avoid this, it is necessary a desaturation maneuver, executed with the help of the magnetorquers.

The model chosen for the reaction wheels is the *OCE-RW40*, which is characterized by the following specifications<sup>[9]</sup>:

$\omega_{max} [RPM]$	$\dot{h}_{max} [Nm]$	$\sigma_{\omega} [RPM]$	$frequency [Hz]$
6000	0.1	2	30

Table 9: Real data for Reaction Wheel

The Simulink model of the reaction wheel takes as input the ideal torque. The  $\dot{\boldsymbol{\omega}}_r$  is computed dividing by the inertia of the wheel around its spin axis.  $\boldsymbol{\omega}_r$  is computed integrating  $\dot{\boldsymbol{\omega}}_r$ .  $-\dot{\mathbf{h}}_r$ , which comes from the control block, is multiplied by the result of the boolean operation  $\boldsymbol{\omega}_r \leq \omega_{max}$ . At this point, the signal passes through a rate limiter and a saturator. It is added a band limited white noise.

## 10. Control logic

The control logic of the satellite is implemented on the computer that handle all the on-board calculations. In particular, all the data from the in-FOV sensors has to be gathered. Then, based on the mission phase, the necessary control has to be calculated and a command has to be sent to the system of actuators. The necessary control calculation is discussed in this section. Clearly, every phase of the mission is somehow different, this could be due to the mission requirements (i.e. detumble or pointing) or to the physical equations that describe the problem (linear or non-linear). Also, when a phase of the mission has to be analyzed and a control applied to it, all the possibilities and limitations coming from sensors and actuators has to be evaluated. As a consequence, the design of a control logic is strictly related to the implementation of the actuators in the system, since even though a perfect control  $\mathbf{u}$  can be designed by placing the fastest poles (in the linear case), then the actuator system will be highly penalized by not being able to perform that torque. As a consequence, it is important to bear in mind that when designing the control logic, always keep in consideration the actuators that will be used.

In the case under analysis, the magnetorquer actuators posses some useful and powerful properties, in particular when they are coupled with a magnetometer, the theory tells that the de-tumbling phase can be easily implemented<sup>[10]</sup>. On the other side, the control for a direction pointing (i.e. Nadir), in the case of magnetorquer is more difficult due to the unpleasant underactuated property of these magnetic systems. Infact, considering the



equation of the actuator for the magnetorquer, and implementing that into the system equations, would result into a instantaneously uncontrollable system as cited in<sup>[11]</sup>. Nevertheless, by following the steps presented in<sup>[11]</sup>, a fully magnetic actuated control can be reached but not without some effort and also drawbacks. In order not to complicate the next discussion, it was chosen the take into consideration also reaction wheels as a secondary actuator system.

In the next sub-sections the logic implemented in the Simulink environment will be presented, then all the more detailed actuator's considerations will be clarified.

### 10.1. De-tumbling phase: the B-dot control

The De-tumbling phase is performed immediately after the release of the spacecraft by the launcher, at this moment the angular velocities are random and depends on the launcher motion, also the attitude is initially unknown. In order to make the satellite ready to enter in the operational regime, so that it can start the pointing of the sensor's targets and the payload, the spacecraft must be de-tumbled. This means to create a control that decelerate the rotational velocities and fetch them to arbitrarily small values.

A frequently adopted option on magnetic-actuated satellites is to implement the so-called *B-dot control*, this method allows to exploit magnetic measurements to produce a direct magnetic dipole command to the magnetorquer which at the end leads to arbitrarily small values of  $\omega$ . The increasing interest on this kind of control law is due to the fact that magnetorquers posses very interesting properties, such as<sup>[10]</sup>:

- absence of catastrophic failure modes (an example of this would be the RW actuators which were characterized by catastrophic failure due to electrostatic charge on the bearing);
- reliable architecture which leads to unlimited operational life;
- the possibility to smoothly modulate the control torque, without inducing coupling with flexible modes (when bang-bang techniques are not adopted);
- significant savings in terms of weight and complexity since no moving parts are present.

Instead, the major drawback of this kind of system is surely the underactuated property. In general, the magnetorquer cannot provide an arbitrarily oriented control torque due to the physical law that rules this device.

$$\mathbf{M}_c = \mathbf{D} \times \mathbf{B}_B \quad (33)$$

Clearly, it doesn't exist a  $\mathbf{D}$  that satisfies the above equation if  $\mathbf{M}_c$  and  $\mathbf{B}$  are parallel. This implies to have, in general, a system that is not controllable at every instant, but it is in an averaged-sense. This implies a major difficulty in implementing a solely magnetic-actuated microsatellite. Avanzini et al.<sup>[10]</sup> demonstrate that asymptotic stability can be obtained through a law of this kind (using only magnetorquer and a magnetometer):

$$\mathbf{D} = -\frac{k_\omega}{\|\mathbf{B}_B\|} \dot{\mathbf{B}}_B \quad (34)$$

The idea of this kind of command is that the variation in magnetic field  $\mathbf{B}$  in the  $\mathcal{B}$  frame can be written as:

$$\dot{\mathbf{B}}_B = \frac{d(\mathbf{A}_{B,N} \mathbf{B}_N)}{dt} = \dot{\mathbf{A}}_{B,N} \mathbf{B}_N + \mathbf{A}_{B,N} \dot{\mathbf{B}}_N \approx \dot{\mathbf{A}}_{B,N} \mathbf{B}_N = -[\omega \times] \mathbf{A}_{B,N} \mathbf{B}_N = -[\omega \times] \mathbf{B}_B \quad (35)$$

The approximation symbol is due to the fact that when  $\omega \gg 1$ , the variation of the magnetic field vector in  $\mathcal{B}$  frame is mainly due to the rotation of the frame and less due to the changing of  $\mathbf{B}_N$  (that is caused by the evolution in the orbital position and other slow variations due to geomagnetic field). With the above equation it has been demonstrated that  $\omega$  and  $\dot{\mathbf{B}}$  are strictly related, so making the control law proportional to  $\dot{\mathbf{B}}$  would be similar to make it proportional to  $\omega$  (like the 'standard' de-tumbling law). This mathematical considerations imply that for a detumbling law, it could be sufficient to have a magnetometer and a magnetorquer without a direct measurement of the angular velocity obtained by a gyro. Another positive consequence of having a proportional law that produces directly a magnetic dipole  $\mathbf{D}$ , is that the command is directly made as an input of the actuator (without inverting any actuator law). It is important to underline that this kind of law would work at his best when angular velocity is high enough to make the assumption of Equation 35 true. In theory the actuated torque is:

$$\mathbf{M}_c = -\frac{k_\omega}{\|\mathbf{B}_B\|} \dot{\mathbf{B}}_B \times \mathbf{B}_B \quad (36)$$

also notice that when  $\omega \gg 1$  Equation 35 is more and more true, and so  $\mathbf{B}_B$  and  $\dot{\mathbf{B}}_B$  are perpendicular, resulting in the maximum actuatable control torque.

Regarding the control law Equation 34, it has to be seen that the vector derived is not the derivative of the magnetic field vector, but it is the derivative of the unit vector of the direction of the magnetic field. Also, notice that all the vector in the above relationship are in the  $\mathcal{B}$  frame since the magnetic field vector  $\mathbf{B}$  comes from the magnetometer measurement.

In the context of the simulation environment on Simulink, the formulation chosen for the b-dot control comes from<sup>[10]</sup> of Avanzini et al work. Some precaution has to be taken when implementing the law, since the numerical derivative of a measured (hence noisy) signal has to be performed. This inconvenience can be overcome by using a low-pass filter<sup>[7]</sup>. In order to make some sense out of the calculation, a discrete low-pass Butterworth filter of the 1st order has been used just after the discrete derivative block. Setting the cut-off frequency on 0.06 rad/s the signal is pretty clean and the results of simulation are coherent. Moreover, the gain value  $k_\omega$  has to be defined. Avanzini et al. extensively discuss this parameter and propose a method for its characterization<sup>[10]</sup>. In particular the indicative formula is the following:

$$k_\omega = 2n(1 + \sin \xi) \min(I_x, I_y, I_z) \quad (37)$$

Where  $n$  represent the mean motion of the orbit,  $\xi$  the inclination of the orbit with respect to the magnetic equator. Notice that during the detumbling the inertia moments are all equal. The value obtained is

$$k_\omega = 0.0363 \text{ kg} \cdot \text{m}^2 \text{s}^{-1}$$

## 10.2. Slew and Nadir pointing phases

### 10.2.1 Control law for the Slew and Tracking Manuever

The goal for the control system at this phase of the mission is to track the  $\mathcal{LVCH}$  frame. In order to obtain the right alignment of the frames, both the attitude error and the angular velocity error should be zero. Infact the tracking of the  $\mathcal{LVCH}$  frame means not only to reduce the error angles but also to arrive at the aligned condition with the correct angular velocity in order to not overshoot the correct position. In this case of control, the attitude error matrix is  $A_{BL}$ , which leads from the  $\mathcal{LVCH}$  to the body frame, and the goal is to make it close to the identity matrix. For this reason, it was desired to make the extra diagonal terms close to zero and the error vector was defined as:

$$\epsilon = (A_{BL}^T - A_{BL})^V \quad (38)$$

The  $[\cdot]^V$  operator is the inverse of  $[\cdot \times]$ , so it maps a skew-symmetric matrix back to its generating vector. The angular velocity error was defined as:

$$\omega_{BL} = \omega - A_{BL}[0 \ 0 \ n]^T \quad (39)$$

For the case under analysis, in which the orbit is slightly elliptical, it would have been more precise to use the true anomaly rate  $\dot{\theta}$  instead of the mean motion  $n$  in Equation 39. It was used  $n$  for simplicity, this doesn't affect the performance of the controller since the orbit is almost circular.  $\omega$  was obtained by taking the numerical derivative of the matrix  $A_{BN}$ , the matrix computed with the attitude determination algorithm, and then inverting the formula:

$$\dot{A}_{BN} = -[\omega \times] A_{BN} \quad (40)$$

Since  $A_{BN}$  is affected by noise, taking its derivative numerically amplifies it, leading to a bad estimation of the angular velocity. Therefore a discrete lowpass Butterworth filter was applied before the computation of  $\omega$ . This was set as a 1st order filter with cut-off frequency at 1 rad/s. Once computed  $\alpha$  and  $\omega_{BL}$  a suitable control law was:

$$M_c = -k_1 \epsilon - k_2 \omega_{BL} \quad (41)$$

This kind of control law is inspired by the linear full-state feedback control  $u = -kx$ . In particular, referred to the linearized Euler equations in which a set of three Euler angles  $\alpha = [\alpha_x \ \alpha_y \ \alpha_z]$  is introduced. This set of small angles represent the misalignment between the  $\mathcal{B}$  and  $\mathcal{LVCH}$  frame. When this linearization is made, the state  $x$  for the state-space formulation, contains  $\alpha$  and  $\dot{\alpha}$ . If the  $u = -kx$  is implemented with that state, the control law becomes a *Proportional-Derivative* control, in the form:

$$M_c = -K_p \alpha - K_d \dot{\alpha} \quad (42)$$

Since the linear control theory allows to use different methodologies to calculate the gains matrices  $K_p$  and  $K_d$ , the linearized control law was firstly analyzed. In particular, the pole placement technique was used, on the following state-space representation of the system.

$$\begin{cases} \dot{x} = Ax + Bu \\ y = Cx + Du \end{cases} \quad A = \begin{bmatrix} 0 & (1-K_x)n & 0 & -n^2 K_x & 0 & 0 \\ (K_y-1)n & 0 & 0 & 0 & -n^2 K_y & 0 \\ 0 & 0 & 0 & 0 & 0 & 0 \\ 1 & 0 & 0 & 0 & 0 & 0 \\ 0 & 1 & 0 & 0 & 0 & 0 \\ 0 & 0 & 1 & 0 & 0 & 0 \end{bmatrix} \quad B = \begin{bmatrix} \frac{1}{I_x} & 0 & 0 \\ 0 & \frac{1}{I_x} & 0 \\ 0 & 0 & \frac{1}{I_x} \\ 0 & 0 & 0 \\ 0 & 0 & 0 \\ 0 & 0 & 0 \end{bmatrix} \quad (43)$$

The first equation of the system represent the state space dynamics, which can be studied for the stability properties, while the second one represents the output coming from the sensors. The open-loop poles calculated for this system were:

$$p_{open} = \begin{bmatrix} 0 \pm 0.0011i \\ 0 \pm 0.0002i \\ 0 \end{bmatrix} \quad (44)$$

The gain matrix  $K = [K_d \ K_p]$  was assessed through the  $place(A,B,p)$  Matlab function that requires the state-space matrices  $A$  and  $B$ , and also the closed-loop poles that are desired  $p$ . At this point, this vector of six poles must be hypotized. Some precautions must be taken when the poles are decided:

- closed-loop poles shall not be too far from the corresponding open-loop poles, since there are constraints on the capabilities of the actuator;
- the real part of the closed-loop poles must be negative in order to guarantee asymptotic stability;
- the imaginary part of the poles should be decided in order to minimize the overshoot;

The chosen poles were:

$$p = \begin{bmatrix} -0.02 \pm 0.1i \\ -0.01 \pm 0.06i \\ -0.05 \pm 0.1i \end{bmatrix} \quad (45)$$

The gain matrix can be used for the linear-control law. For simplicity, it wasn't used a matrix for the non-linear control but only a scalar, in particular it was selected the order of magnitude of the gain matrix from linear control just calculated. The values for the gains were then refined with trial and error. The response of the system was satisfactory with the following values:

$$k_1 = 0.001 \text{ kg} \cdot \text{m}^2 \text{s}^{-2} \quad k_2 = 0.6 \text{ kg} \cdot \text{m}^2 \text{s}^{-1}$$

### 10.2.2 Actuator command logic for Slew and Nadir pointing

Once the control torque  $M_c$  has been calculated, a logic was implemented to translate it into a command to be sent to the actuators. Magnetic actuators generate the torque with the formula

$$M = -[B \times]D \quad (46)$$

where  $[B \times]$  is the skew symmetric matrix obtained applying the  $[\cdot \times]$  operator to the magnetic field vector in body frame, measured by the magnetometer. However, it isn't possible to compute  $D$  by inverting Equation 46 because  $[B \times]$  is singular. This reflects the fact that is never possible to generate three independents components of the control torque, since  $M$  is always perpendicular to both  $D$  and  $B$ . One possible solution is to add one or more reaction wheel(s). It was chosen to add two reaction wheels, one along  $x_B$  and one along  $y_B$  of the  $B$  frame. This because, as it is shown in Equation 48 and Equation 49, when only one reaction wheel is used, the matrix of the linear system necessary to be solved, becomes singular when the component of the magnetic field aligned with the reaction wheel is zero. As shown in Figure 6 all components of the magnetic field will go to zero at a certain point. If just one reaction wheel would be used, it should be disactivated when the respective component of  $B$  goes to 0. This would mean that at certain instants of time, the only actuators that can operate are the magnetorquer. This would lead to the undeterminate problem of defining a command to the magnetoactuator Equation 34.

Following the considerations given just above, the command is always given in the form:

$$cmd = [D_x \ D_y \ D_z \ -\dot{h}_x \ -\dot{h}_y]^T \quad (47)$$

where  $D_x$ ,  $D_y$  and  $D_z$  are the dipoles to be given by the magnetic actuators,  $\dot{h}_x$  and  $\dot{h}_y$  are the moments to be given by the reaction wheels.

Only one reaction wheel is used at a time, they are never used all at once. A logic was implemented to choose which reaction wheel to use. It consists in an if/else construct, implemented in Simulink through two enabled subsystems, which takes as condition that  $|B_x| \geq 10^{-5} \text{ T}$ . If the condition is satisfied, the reaction wheel along x is used and the linear system reported below is solved,

$$\begin{bmatrix} 1 & B_z & -B_y \\ -B_z & 0 & B_x \\ B_y & -B_x & 0 \end{bmatrix} \begin{bmatrix} -\dot{h}_x \\ D_y \\ D_z \end{bmatrix} = \begin{bmatrix} M_x \\ M_y \\ M_z \end{bmatrix} \quad (48)$$

The command vector is assembled as indicated in Equation 47 by taking the solution Equation 48 and setting to zero  $D_x$  and  $\dot{h}_y$ . If the condition is not satisfied, the reaction wheel along y is used, the linear system to be solved is

$$\begin{bmatrix} 0 & B_z & -B_y \\ -B_z & 1 & B_x \\ B_y & -B_x & 0 \end{bmatrix} \begin{bmatrix} D_x \\ -\dot{h}_y \\ D_z \end{bmatrix} = \begin{bmatrix} M_x \\ M_y \\ M_z \end{bmatrix} \quad (49)$$

and the command vector is assembled as indicated in Equation 47 by taking the solution of Equation 49 and setting to zero  $D_y$  and  $\dot{h}_x$ . The idea behind this kind of logic was to be always able to compute the command vector. Indeed, the matrix of Equation 48 is singular when  $B_x = 0$  T and the matrix of Equation 49 is singular when  $B_y = 0$  T. It is clear that, using this kind of logic, it is always possible to compute a command to be sent to the actuators. The assumption that was made is that at every instant of time, at least one of  $B_x$  and  $B_y$  is non zero. Looking at the graph in figure Figure 6, it can be noticed that, when  $B_x$  is zero,  $B_y$  is far from zero and vice-versa. It wasn't chosen to put the second reaction wheel along z axis because, as it is shown in the graph reported in the same figure,  $B_z$  is always around the zero value. That condition would generate a high-valued command to the reaction wheels and to the dipoles. Hence, the saturation would happen earlier.

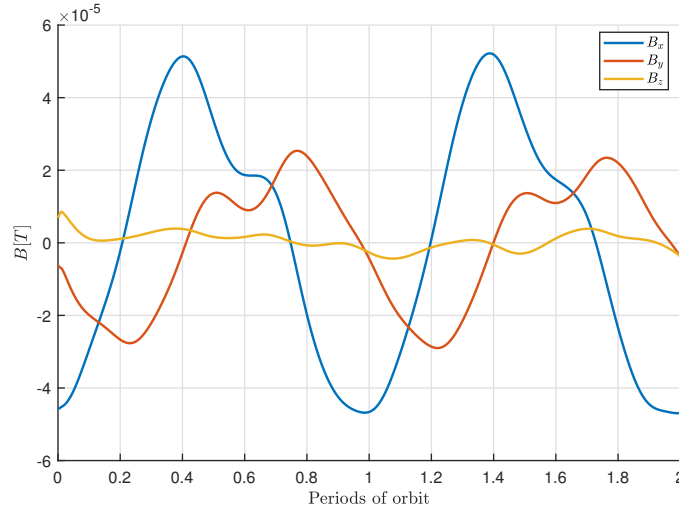


Figure 6: Magnetic Field in  $B$  frame

## 11. Simulation results

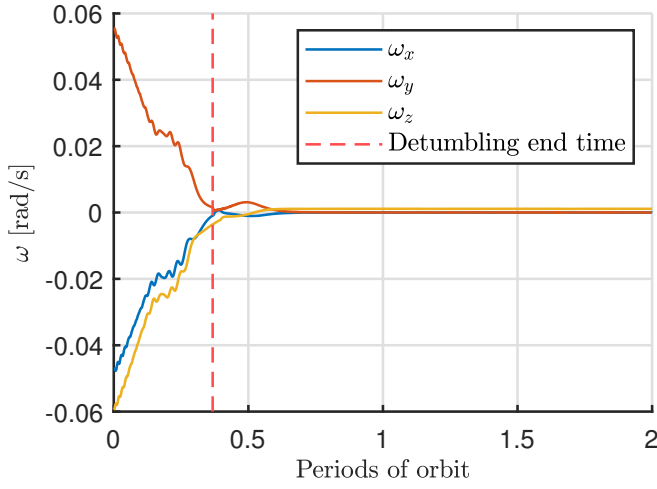
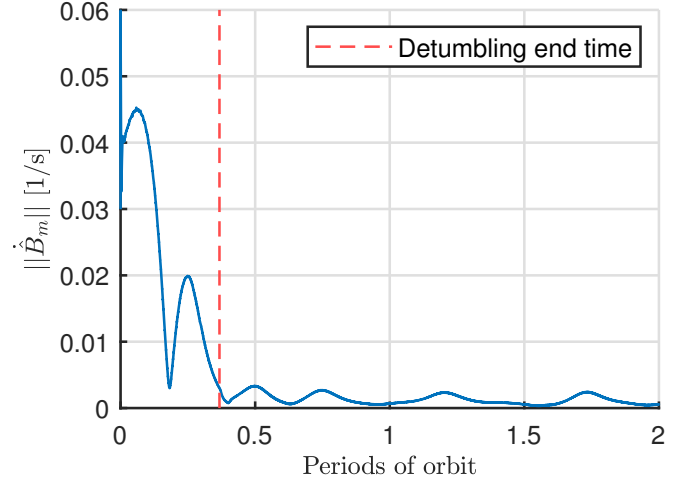
In the present section, the results of the simulation will be presented and discussed. The simulation has been executed for a period of two complete orbits in order to observe all the three main phases of the satellite's mission. It has been started from random initial conditions on both angular velocity  $\omega$  and Euler angles  $s$ . The  $\omega$  components were limited in range  $-0.06 \div 0.06$  rad/s, while  $s$  components were in range  $0 \div 2\pi$  rad.

Since the final mission of the satellite is Nadir pointing, particular attention is posed on the values of some physical quantities, in particular:

- $\omega$  and  $\|\dot{\mathbf{B}}_m\|$  for the detumbling phase;
- $\alpha$  and  $\omega_{BL}$  for the slew and tracking phase, where  $\alpha = \frac{1}{2} (\mathbf{A}_{BL}^T - \mathbf{A}_{BL})^V$ .

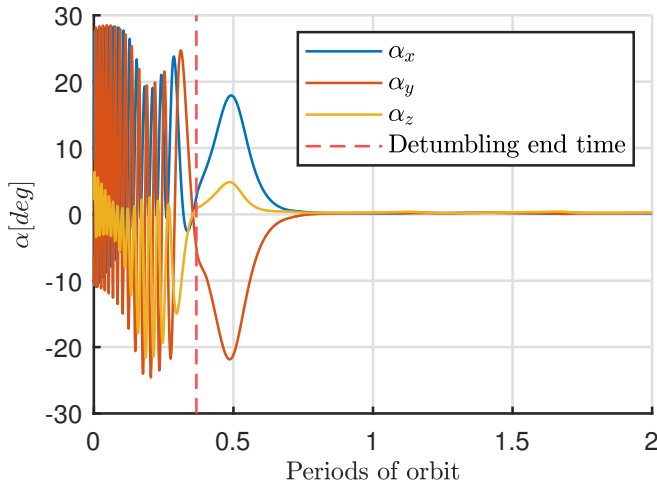
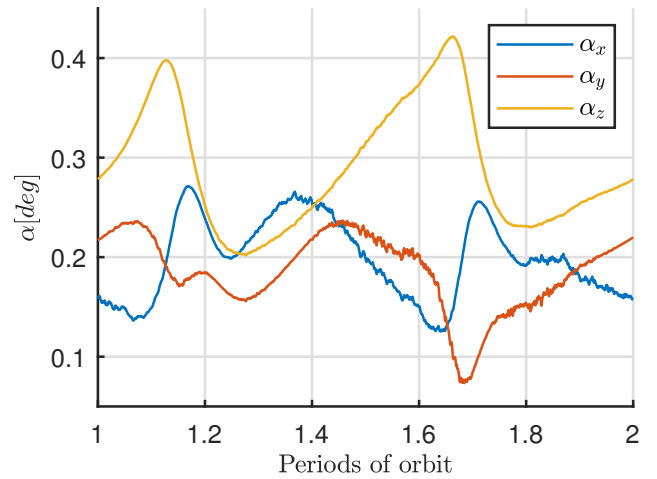
Furthermore, from the satellite operational point of view, some other physical quantities are relevant, such as the measured magnetic field  $\mathbf{B}_m$  and the computed values like the evaluated attitude matrix  $\mathbf{A}_{BN,sens}$  and the control torques  $\mathbf{M}_c$ . In addition, the angular velocities of the reaction wheels and the magnetorquers' generated dipoles will be analyzed to verify the saturation condition and the consumption power respectively.

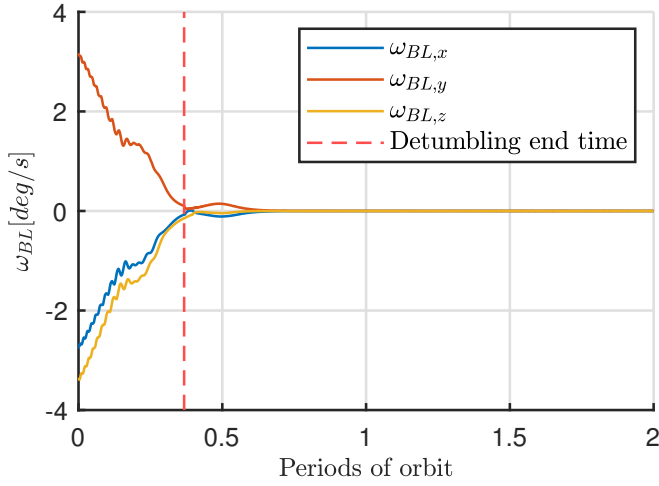
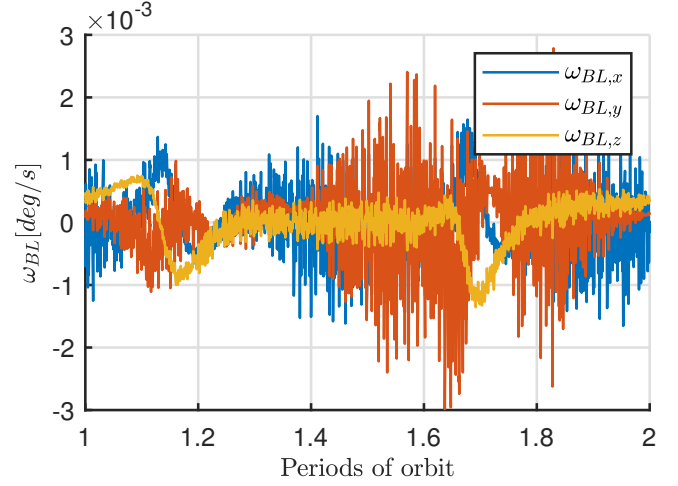
### 11.1. Detumbling analysis

Figure 7:  $\omega$  in  $\mathcal{B}$  frameFigure 8:  $\|\dot{\mathbf{B}}_m\|$  in  $\mathcal{B}$  frame

As it can be seen in Figure 7 and Figure 8, the detumbling has a duration of less than half orbit, then the slew and tracking control engages to keep the angular velocity stabilized. Note that from this particular case nothing general can be deduced, as the period and the behaviour of the detumbling phase strongly depends on the initial conditions of the satellite and also on the condition on which the control switch to the next phase. In this simulation, this criteria is based on the evaluation of  $\|\dot{\mathbf{B}}_m\|$ . Looking at the graph in Figure 8, the detumbling phase ends when the condition  $\|\dot{\mathbf{B}}_m\| < 0.003 \text{ s}^{-1}$  is satisfied.

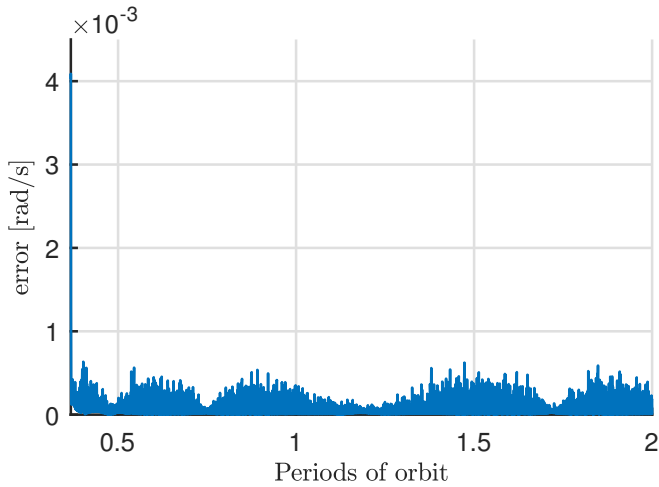
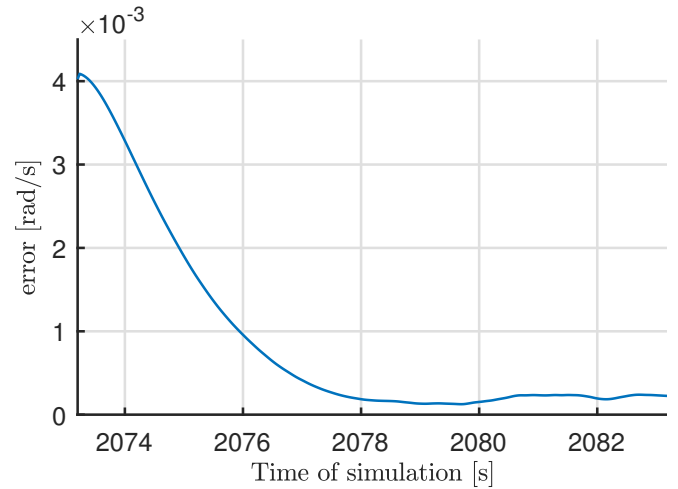
### 11.2. Slew and tracking phase analysis

Figure 9: Attitude error  $\alpha$ Figure 10: Zoom on  $\alpha$

Figure 11: Angular velocity error  $\omega_{BL}$ Figure 12: Zoom on  $\omega_{BL}$ 

In Figure 9 and Figure 11 it can be seen that, after the detumbling, there is a transient after which both attitude and angular velocity errors converge to zero in a short period of time and keep stabilized. To better evaluate the errors in the tracking phase, in Figure 10 and Figure 12 a zoom on the final phase can be appreciated. The high frequency oscillations are mainly imputed to errors introduced by sensors and actuators. Indeed, both the command to the actuators and the executed control action are affected by noise.

It can be noticed from Figure 9 and Figure 11 that, at the beginning of slew manoeuvre, both attitude and angular velocity errors increase before going towards zero. This can be explained by Figure 14, in which the estimation of the angular velocity done by the algorithm presented in subsection 10.2.1 is initially rough as it comes from the numerical derivation of  $A_{BN}$ .

Figure 13:  $\|\omega_{estim} - \omega\|$  after detumblingFigure 14:  $\|\omega_{estim} - \omega\|$  in the first 10 s after detumbling

As can be seen in Figure 13, after the error in estimated angular velocity decreases it stabilizes itself toward values close to zero.

### 11.3. Control action analysis

Another important perspective to consider is how the actuators behave during the simulation, in particular verifying the torque generated and the reached saturation levels. For this last point, it can be evaluated whether a desaturation algorithm becomes necessary to be implemented on the reaction wheels. For the dipoles, this analysis could be useful to dimension the energy supply (i.e. the solar panels and batteries).

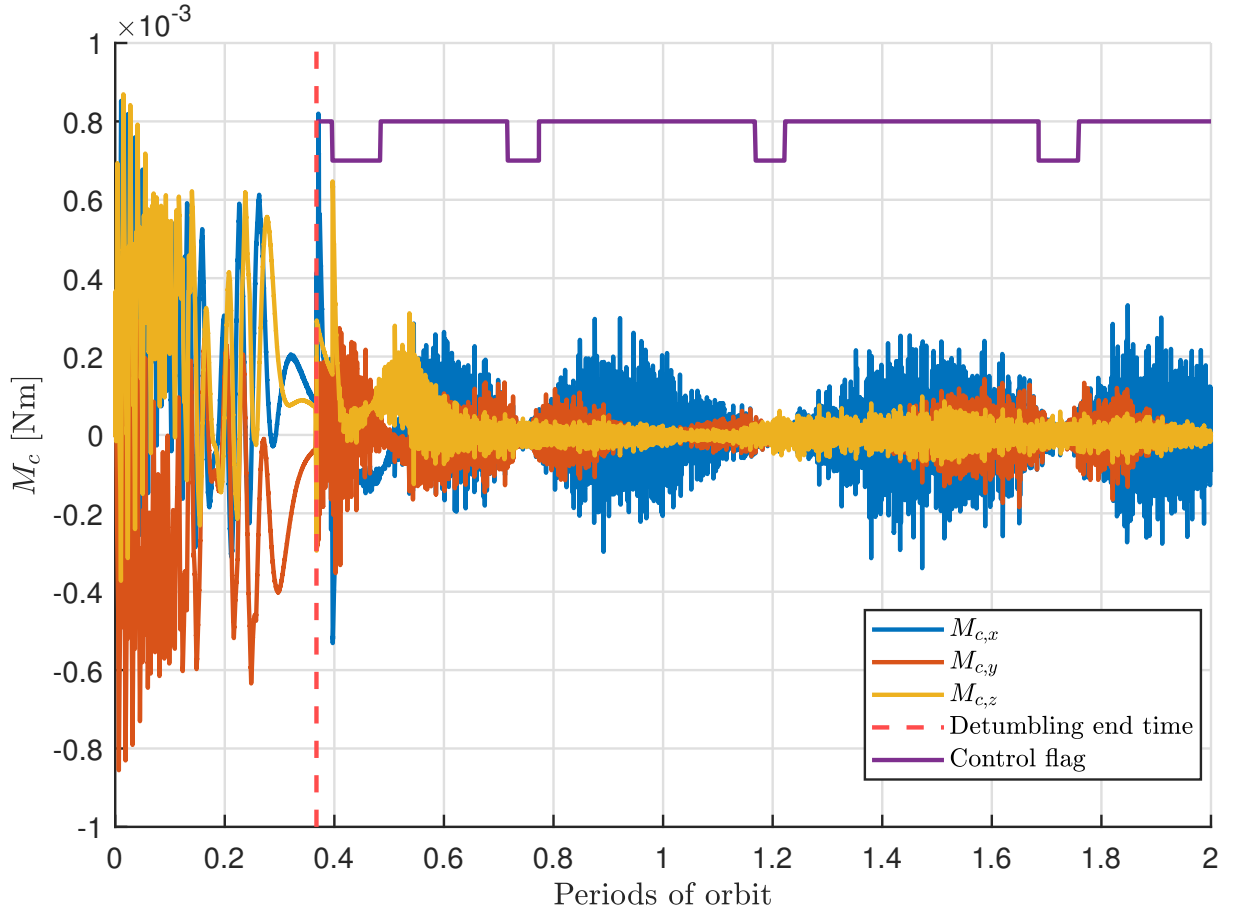


Figure 15: Actuated torque and control logic flag on reaction wheels

From Figure 15 it can be noticed that the torque is greater but much less noisy on detumbling phase than the tracking phase. Indeed, the control action during the first phase is calculated basing on the information coming only from the magnetometer, which is far more accurate than the other sensors (Table 6). Right after the detumbling phase, the slew manoeuvre presents a peak on the control torque requested. It is imputable to the bad estimation on the angular velocity on the starting phase, as seen in Figure 14.

During the tracking phase, a low-frequency harmonic can be detected in the control moment, which is most noticeable on the x component. This behaviour can be related to the activation of the reaction wheel on the same axis, as can be seen from the control flag. It can also be seen that the time of activation of the wheel on x axis is longer than that on y axis. A possible alternative to this implementation could involve a better load distribution between the reaction wheels, again taking into account the variation in the magnetic field which rules the control logic.

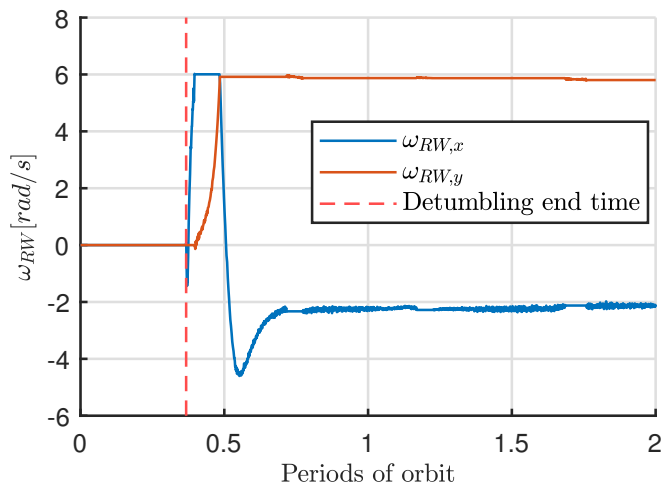


Figure 16: Angular velocities of RW

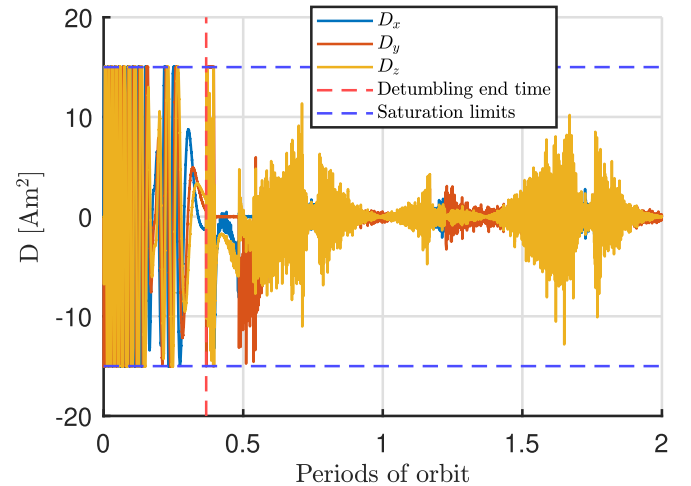


Figure 17: Dipole of magnetic coils



In [Figure 16](#) is shown the angular velocities of the two reaction wheels. The saturation rates ([Table 9](#)) are much bigger in absolute value with respect to the values reached during the simulation. The [Figure 17](#) shows instead the magnitude of the magnetic dipoles along the three axis. The most critical phase for the magnetorquer is surely the detumbling phase since the control torque is relatively high (as noted in [Figure 15](#)) and magnetorquer is the only actuator used. It can be observed that the value of the dipole components saturate almost constantly. Since the dipole supplied by the magnetorquer is directly proportional to the current, the batteries must be sized in order to supply the required energy during the phase with retracted solar panels.

## Bibliography

- [1] ESA. Esail maritime satellite launched. Website, 2020. Site: [https://www.esa.int/Applications/Connectivity\\_and\\_Secure\\_Communications/ESAIL\\_maritime\\_satellite\\_launched](https://www.esa.int/Applications/Connectivity_and_Secure_Communications/ESAIL_maritime_satellite_launched).
- [2] Howard D. Curtis. *Orbital Mechanics for Engineering Students*. Elsevier, 2014.
- [3] ESA. Types of orbits. Website, 2020. Site: [https://www.esa.int/Enabling\\_Support/Space\\_Transportation/Types\\_of\\_orbits](https://www.esa.int/Enabling_Support/Space_Transportation/Types_of_orbits).
- [4] James R. Wertz. *Spacecraft Attitude Determination And Control*. Kluwer Academic Publishers, 1978.
- [5] Meisei. Horizon sensor. Website, 2020. Site: <https://www.meisei.co.jp/english/products/space/satellite-components/p1380>.
- [6] AAC ClydeSpace. Sun sensor. Website, 2021. Site: <https://www.aac-clyde.space/what-we-do/space-products-components/adcs/ss200>.
- [7] John I. Crassidis F. Landis Markley. *Fundamentals of Spacecraft Attitude Determination and Control*. Springer, 2014.
- [8] AAC ClydeSpace. Magnetorquer. Website, 2021. Site: <https://www.aac-clyde.space/what-we-do/space-products-components/adcs/mtq800-10>.
- [9] O.C.E. Technologies. Rw40. Website, 2022. Site: <https://satsearch.co/products/oce-technology-rw40-reaction-wheel-4nms>.
- [10] Giulio Avanzini, Fabrizio Giulietti. Magnetic Detumbling of a Rigid Spacecraft. *Journal of Guidance, Control and Dynamics*, 35(4):1326–1333, 8 2012.
- [11] M. Lovera, A. Astolfi. Spacecraft attitude control using magnetic actuators. *Elsevier*, 40(4):1405–1414, 2 2004.